

An experimental study on the magnetic field permeability of an inductive-pulsed plasma thruster

Bi-Xuan Che(车碧轩), Jian-Jun Wu(吴建军), Mou-Sen Cheng(程谋森), Xiao-Kang Li(李小康), Yu Zhang(张宇), and Da-wei Guo(郭大伟)

Citation: Chin. Phys. B, 2025, 34 (**2**): 025203. DOI: 10.1088/1674-1056/ad9e95
Journal homepage: http://cpb.iphy.ac.cn; http://iopscience.iop.org/cpb

What follows is a list of articles you may be interested in

Power transfer efficiency in an air-breathing radio frequency ion thruster

Gao-Huang Huang(黄高煌), Hong Li(李宏), Fei Gao(高飞), and You-Nian Wang(王友年)
Chin. Phys. B, 2024, 33 (**7**): 075201. DOI: 10.1088/1674-1056/ad426c

Interaction between plasma and electromagnetic field in ion source of 10 cm ECR ion thruster

Hao Mou(牟浩), Yi-Zhou Jin(金逸舟), Juan Yang(杨涓), Xu Xia(夏旭), and Yu-Liang Fu(付瑜亮)
Chin. Phys. B, 2022, 31 (**7**): 075202. DOI: 10.1088/1674-1056/ac4906

Investigation on plasma structure evolution and discharge characteristics of a single-stage planar-pulsed-inductive accelerator under ambient fill condition

Xiao-Kang Li(李小康), Bi-Xuan Che(车碧轩), Mou-Sen Cheng(程谋森), Da-Wei Guo(郭大伟), Mo-Ge Wang(王墨戈), and Yun-Tian Yang(杨云天)
Chin. Phys. B, 2020, 29 (**11**): 115201. DOI: 10.1088/1674-1056/ab9f2a

Research of influence of the additional electrode on Hall thruster plume by particle-in-cell simulation

Xi-Feng Cao(曹希峰), Hui Liu(刘辉), Da-Ren Yu(于达仁)
Chin. Phys. B, 2020, 29 (**9**): 095204. DOI: 10.1088/1674-1056/aba2e3

Particle-in-cell simulation for the effect of magnetic cusp on discharge characteristics in a cylindrical Hall thruster

Sheng-Tao Liang(梁圣涛), Hui Liu(刘辉), Da-Ren Yu(于达仁)
Chin. Phys. B, 2018, 27 (**4**): 045201. DOI: 10.1088/1674-1056/27/4/045201

An experimental study on the magnetic field permeability of an inductive-pulsed plasma thruster

Bi-Xuan Che(车碧轩), Jian-Jun Wu(吴建军)†, Mou-Sen Cheng(程谋森), Xiao-Kang Li(李小康), Yu Zhang(张宇), and Da-Wei Guo(郭大伟)

College of Aerospace Science and Engineering, National University of Defense Technology, Changsha 410073, *China*

(Received 22 August 2024; revised manuscript received 6 December 2024; accepted manuscript online 13 December 2024)

Inductive-pulsed plasma thruster is an in-space propulsion device that generates thrust by ionizing and accelerating plasma through pulsed electromagnetic field. In this paper, the correlation between plasma structure evolution and magnetic field permeability is studied using a B-dot probe array system, combing with high-speed camera and electrical parameter measurement. Further discussions explained the mechanism how the magnetic permeation characteristics affect the energy deposition between circuit and plasma.

Keywords: inductive-pulsed plasma thruster, electric propulsion, B-dot probe, plasma structure

PACS: 52.75.Di, 52.80.–s, 52.70.–m, 84.30.Ng

DOI: 10.1088/1674-1056/ad9e95 **CSTR:** 32038.14.CPB.ad9e95

1. Introduction

Inductive-pulsed plasma thruster (IPPT), also known as pulsed inductive thruster (PIT), is a sort of electric propulsion device that generates thrust by ionizing and accelerating gaseous propellant through a pulsed inductive electromagnetic (EM) field.[1] Owes to its megawatt power capability, wide propellant compatibility, and wide range thrust regulation ability,[2] IPPT becomes a promising candidate for future nuclear electric propulsion,[3] and low-orbit air-breathing electric propulsion.[4]

Despite over 50 years' development, IPPT has not yet been tested in space. On one hand, the life time of components such as pulse valve and pulse switch are not sufficient, on the other hand, the performance of the thruster is not yet reliable.[5] The TRW developed IPPT-type thruster PIT Mark-I ($I_{sp} = 1897$ s, $\eta = 29\%$)[6] and PIT Mark-Va ($I_{sp} > 5000$ s, $\eta = 50\%$)[7] both achieved impressive propulsive performance, but their respective successors, the PIT Mark-IV ($I_{sp} = 820$ s, $\eta = 15\%$)[8] and PIT Mark-VI ($I_{sp} = 2750$ s, $\eta = 19\%$),[9] neither achieve comparable performance respectively. Those facts supply that the understanding on the efficient acceleration mechanism of plasma in IPPTs is still unclear.

To find out the reasons for the performance difference between PIT Mark-I and PIT Mark-IV, Lovberg compared the radial magnetic field B_r at different coaxial positions along the center line between inner and outer diameter of drive-coil. The result showed that the axial permeability of coil magnetic field in PIT Mark-I is obviously weaker than that in PIT Mark-IV. Lovberg believed that the magnetic field penetration would not only weaken the electromagnetic force on the plasma, but also reduce the utilization of the propellant, resulting in the so-called snowplow loss.[10]

More recently, in an IPPT-type device named Faraday accelerator with radio frequency assisted discharge (FARAD), Polzin measured the B_r curves at two different axial locations. The data was compared with PIT Mark-Va and the result indicated that, within the early few μs, the axial penetration of the magnetic field in FARAD is more obvious than PIT Mark-Va. Polzin concluded that, IPPT with low discharge energy tends to occur a delayed gas breakdown, which subsequently leads to serve energy dissipation through circuit resistance and plasma resistance.[11] Little implemented a theoretical analysis of the magnetic field permeability characteristics of the current sheet by embedding a one-dimensional magnetic field permeability equation into the electromechanical model. The calculation results show that the magnetic-impermeable state can only be achieved over certain specific ionization ratio is achieved.[12]

Conclusively, the magnetic field permeation in plasma makes an important effect on the ionization and acceleration process of propellant. This effect might vairy with the discharge process and be influenced by the neutral gas distribution, the plasma ionization degree and the electric parameters of drive-circuit. However, two relevant fundament questions still remain unclear. Namely, how the plasma structure works on the magnetic field permeability, and how the magnetic field permeability influences the energy deposition and conversion between circuit and plasma.

In this study, a transient magnetic field diagnostic system utilizing B-dot probe arrays is developed and calibrated.

†Corresponding author. E-mail: jjwu@nudt.edu.cn

© 2025 Chinese Physical Society and IOP Publishing Ltd. All rights, including for text and data mining, AI training, and similar technologies, are reserved.

An in-depth study on the relationship between plasma structure evolution and magnetic field penetration under varied operational parameters is accomplished. Further analysis correlates the magnetic field diagnose, high-speed photographing, and electrical parameter measurement results. The mechanism about how magnetic permeability affects the plasma energy deposition and macroscopic kinetic energy conversion is also explained.

2. Experiment setup and method

As shown in Fig. 1, the experiment system primarily consists of a laboratory IPPT prototype, a discharge chamber, relevant measurement, and control devices. The IPPT prototype includes a planar drive-coil wound by multi spiral conductors, a pulse switch and a capacitor group. More details have been introduced in an earlier study.[14] The plasma region in front of the drive coil is separated from atmosphere by a transparent PMMA tube. During experiment, only the discharge chamber is vacuumed, while the propellant argon is fed through the bottom flange.

The temporal plasma structure is captured by a high-speed camera (Phantom V2012). The exposure time of the camera is 0.9 μs and the sampling rate is around 66 kHz, which results in a sampling interval about 1.5 μs. The circuit current I_c is detected by a Rogowsky coil (Pearson 5046) and the capacitor voltage V is measured by a high voltage probe (Tektronix P6015A).

In order to concentrate the induced Lorentz force on axial direction, the conductors of drive-coil are carefully wounded so that the axial component of magnetic field is neglectable. Meanwhile, since the thruster is axisymmetric, the angular component is also neglectable. Therefore, only the radial component B_r of magnetic field intensity is investigated in this study. The time-varying curves of B_r at different axial locations z along the midline of drive-coil are measured by a B-dot probe array-based magnetic diagnostic system.

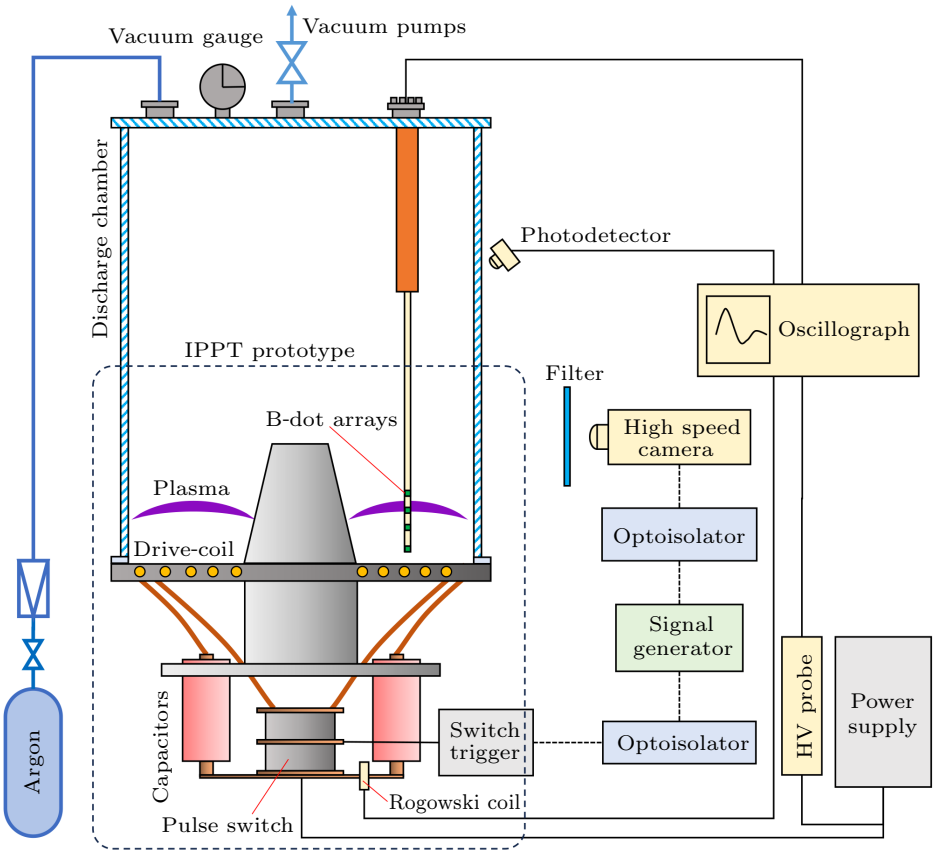


Fig. 1. Experimental setups.

2.1. Magnetic field diagnostic system

The transient magnetic field diagnostic system is shown in Fig. 2. The probe array contains 8 sampling coils whose interval is 1.5 cm. Commercial micro inductor chips (812SMS-R12GLC) are used as the sampling coil to improve the consistency between probe arrays. A printed circuit board is designed as the skeleton of inductor chips to improve the accuracy of direction and location. The probe signal is transmitted by 0.3-mm diameter coaxial cables commonly used in mobile phone RF antenna. An RC integration circuit shown in Fig. 3 is used to integrate the original probe signals. The probe assembly is encapsulated in a 5-mm diameter quartz glass tube to protect the inductor chips from plasma erosion, small enough

to distinguish the spatial features of the plasma current sheet, whose thickness was several centimeters reported in Ref. [10].

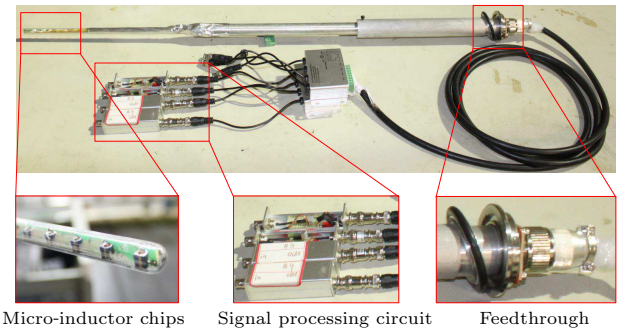


Fig. 2. Transient magnetic field diagnostic system.

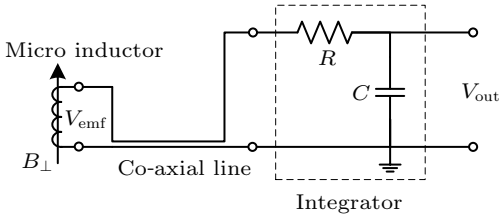
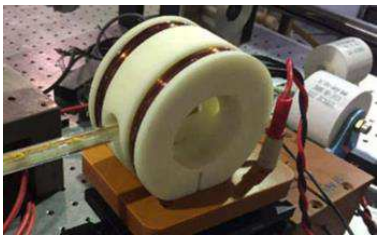


Fig. 3. Signal processing circuit.

2.2. Probe calibration system

Due to the geometric errors of inductor chips, as well as the stray capacitance and inductance of the transmission line, the actual B-dot probe coefficient nA (n is the number of turns of single inductor chip and A is the cross section of each turn) usually deviates from its theoretical value and relies on the field frequency f. Considering this, the probe needs to be calibrated within the designed operating frequency range.[13]

A Helmholtz coil is used to provide the standard and uniform magnetic field for probe calibration. Apparently, the frequency response character (FRC) of Helmholtz coil itself should exceed the probe chip, and the size of uniform area of the standard field needs to be larger than the probe chip size, as well. However, those two requirements turn out to be conflict and after several attempts, a high frequency Helmholtz coil as shown in Fig. 4 is accomplished. The radius r_H equals 36 mm while the number of turns n_H is 40.



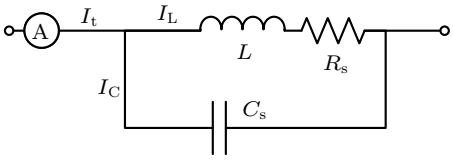


Fig. 4. Photograph and equivalent circuit of the Helmholtz coil.

The actual equivalent circuit of Helmholtz coil is shown in Fig. 4, where C_s, L_H, and R_s represent the stray capacitance, stray resistance, and self-inductance, respectively. The current meter A measures the total current I_t, including the displacement current I_C passing through C_S and the conduction current I_H passing through L and R_s, of which only I_H can generate the standard calibration magnetic field. The FRC of Helmholtz coil is tested using a signal generator. According to the circuit waveforms of IPPT, the nature period of each discharge is around 10 μs, whose corresponding frequency is 100 kHz. To capture the detailed features of discharge, the characteristic frequency is expanded to 10 kHz–500 kHz. It can be seen from Fig. 5 that the operating frequency range of Helmholtz coil is about 0 MHz–1 MHz, entirely covering the characteristic frequency of the magnetic field in IPPTs. The axial and radial distribution (see Fig. 6) of the standard field is measured using a Gauss meter. As shown in Fig. 7, the magnetic field generated by Helmholtz coil has a good uniformity within the size range of the probe inductor coil.

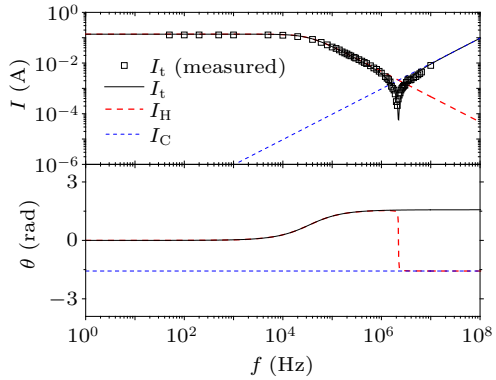


Fig. 5. Frequency response characteristic (FRC) of Helmholtz coil.

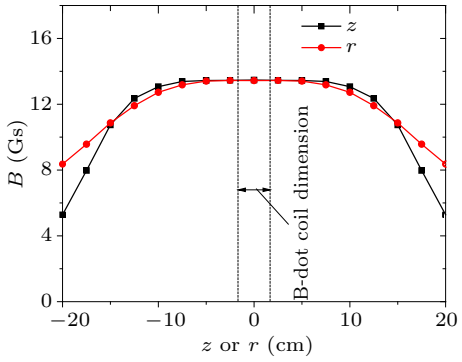


Fig. 6. The axial and radial distributions of the field generated by Helmholtz coil.

A schematic diagram of the calibration system is shown in Fig. 7, where an RLC pulse circuit is used to generate the exciting current. The frequency is adjusted by changing different valued capacitors. The calibration results of all the four adopted B-dot coils are shown in Fig. 8 where competent consistence between inductor coils and varied field frequencies are confirmed. Identical nA value equaling 5.9×10^{-5} m^2 is adopted for all the four B-dot coils, with a relative error of about 5%.

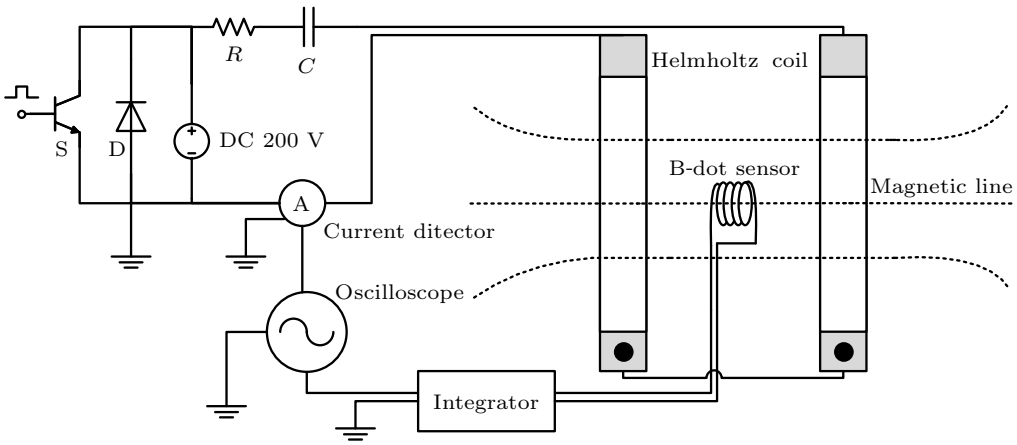


Fig. 7. Probe calibration system.

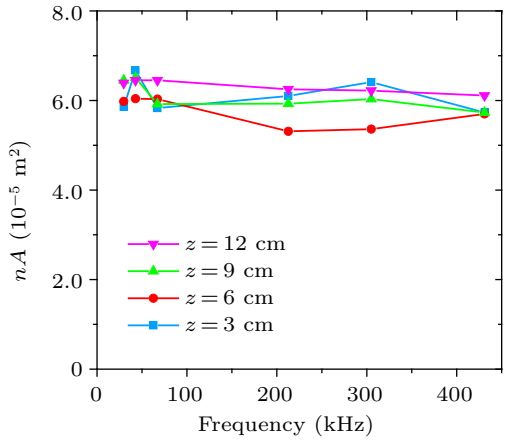


Fig. 8. Probe calibration results.

3. Experiment results

Firstly, the thruster is operated under atmosphere to obtain the unloaded discharge characteristics as a contrast. After that, loaded discharge is investigated using argon as propellant, under varied initial capacitor voltage V_0 and ambient fill gas pressure p_0.

3.1. Unloaded discharge results

The unloaded circuit current I_c waveforms under varied V_0 are shown in Fig. 9.

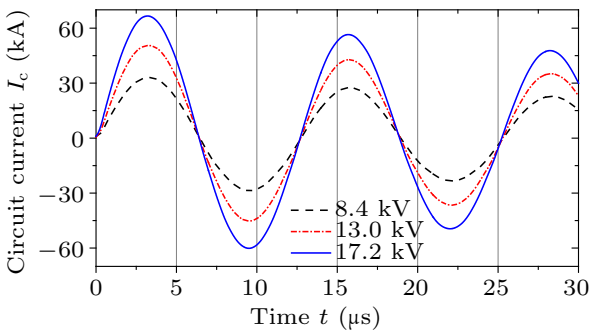


Fig. 9. Unloaded I_c curves under varied V_0.

It can be seen that I_c exhibit obvious underdamped sinusoidal trend owes to its RLC self-excited oscillation nature. The peak value of I_c drops with V_0, while the periods under different V_0 values are exactly identical, equaling about 12.6 μs.

The B-dot array is initially adopted to measuring the radial magnetic field intensity B_r at four different axial locations along the central line of drive coil, which is marked in Fig. 10.

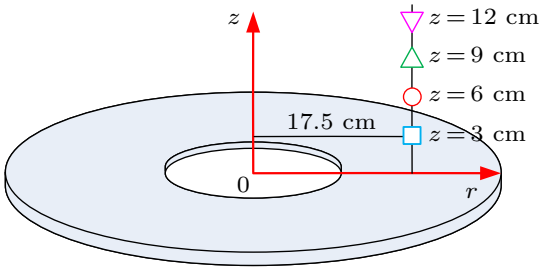


Fig. 10. The locations of B-dot probes.

The results of $V_0 = 17.2$ kV are provided in Fig. 11. It is apparent to see that, although the amplitudes of B_r curves at four different axial positions are different, their time-dependent feature are all consistent with I_c.

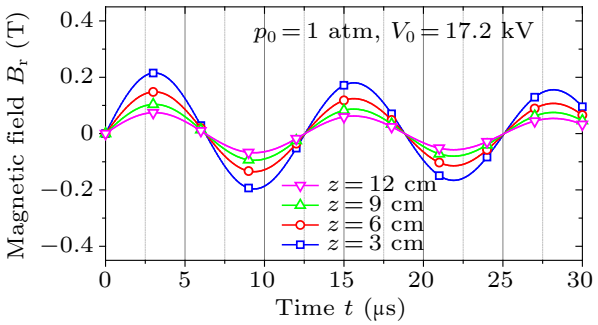


Fig. 11. The unloaded B_r curves at different values of z. The unit 1 atm = 1.01325×10^5 Pa.

Connecting the B_r values at different z at the same time in Fig. 12, it can be seen that the magnetic field strength of the drive-coil decreases exponentially along the axial direction. At $z = 3$ cm, the field intensity achieves about 0.21 T, while at $z = 12$ cm, remains about 0.07 T.

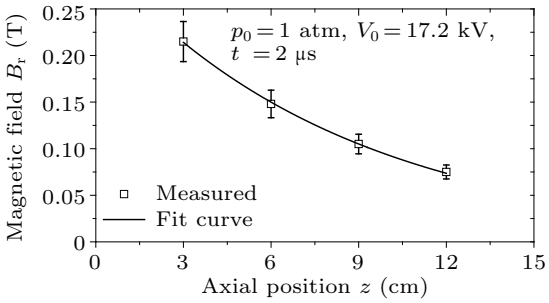


Fig. 12. Unloaded B_r magnitude at different z.

3.2. Loaded discharge results

When p_0 drops to around 10 Pa, a bright breakdown of neutral gas can be seen in the discharge chamber. Figure 13 provides the B_r curves at four positions ($z = 3$ cm, 6 cm, 9 cm, 12 cm) along the midline of drive-coil. The results of $p_0 = 10/20$ Pa and $V_0 = 8.4$ kV/13.0 kV/17.2 kV are compared. For the convenience of analysis, high-speed photographs at six typical instant ($t = 1.5$ μs/4.5 μs/7.5 μs/10.5 μs/13.5 μs/16.5 μs) are attached in the figure, while the positions of the B-dot coils are marked by different symbols and colors. Since the magnetic field is initially induced by drive-coil, the circuit current I_c waveforms are also attached in the plots as contrast.

Comparing any of the loaded B_r curves in Fig. 13 with unloaded curves in Fig. 11, it is apparent to see that the magnetic field strength at different axial positions no longer decay exponentially when plasma emerges, and the time traces of different positions are no longer synchronized with each other, either.

The high-speed photograph indicates the radiation intensity distribution of the plasma. Though the plasma in the thruster is initially produced by the gas breakdown driven by angular electric field, during most of the time of discharge process, the ionization is dominated by the Ohm's heating of plasma current density. Relevant numerical researches have demonstrated that the plasma is approximately in a local thermal equilibrium (LTE) state, so the radiation intensity distribution (namely the high-speed photograph) can be used to indicate the distribution of both plasma density, plasma ionization rate and plasma current density.[12] The plasma current sheet is such a compound structure that carries most of the plasma mass, plasma current density, as well as electrons and ions.

Owes to the highly conductive nature of plasma current sheet, magnetic field induced by drive-coil is screened by the current sheet. This effect strengthens the field between drive-coil and current sheet, while weakens the field beyond current sheet. As a result, notable departure of magnetic field magnitude and phase occurs on the two sides of current sheet. This effect can be seen from the comparison between unloaded discharge (Fig. 11) and loaded discharge (Fig. 13(c)).

At $t = 4$ μs, the field intensity at $z = 3$ cm is about 0.22 T under unloaded discharge while 0.4 T under loaded discharge, showing an notable field compression effect; at the same time, the field intensity at $z = 12$ cm is about 0.06 T under unloaded discharge while nearly 0 T under loaded discharge, showing an effective screening effect. Contrasting the high-speed photograph in Fig. 13(c), it can be seen that $z = 3$ cm and $z = 12$ cm located on the two sides of the of the plasma current sheet. With the axial movement of plasma current sheet, the departures of the field at different locations change with the relative position of current sheet. At $t = 16.5$ μs, when the current sheet has moved beyond the highest probe. The field strength of all the 4 locations rises to around 0.1 T–0.2 T under the compression effect of current sheet.

It should also be noticed that, between the plasma current sheet and drive-coil, even though a strong EM field still exists, a dark region with hardly any gas ionization is observed. This fact supplies that, in this region, the gas density is extremely low that no sufficient atoms for ionization. In other words, the plasma current sheet has taken away almost all the gas it sweeps.

As shown in case-1, B_r at $z = 3$ cm presents an oscillation characteristic similar to the I_c waveform, while B_r at both $z = 6$ cm and 12 cm is much smoother, indicating that the plasma current sheet has partially screened the magnetic field induced by drive-coil. Compared with the high-speed photos, it can be seen that the discharge area of the plasma is obviously more dispersed in this case. On the top of ionization region, crown-like plasma branches indicate an ununiform ionization of gas. At $t = 7.5$ μs, the plasma structure has shrunk a little and as a result, the magnetic field at $z = 3$ cm is obviously higher than other positions, indicating that the magnetic field screening effect has become stronger.

In case-2, V_0 is increased to 13.2 kV and p_0 remains 10 Pa. At $t = 1.5$ μs, the B_r separation between $z = 3$ cm and other three locations have increased compared with case-1. This fits the fact that a more compact plasma current sheet is formed closely above $z = 3$ cm. Keep raising V_0 to 17.2 kV, at $t = 1.5$ μs, B_r at $z = 6\backslash 9\backslash 12$ cm almost drop zero while B_r at $z = 3$ cm nearly achieves 0.1 T, which supplies that a high-quality magnetic-impermeable plasma current sheet has established between $z = 3$ cm and 6 cm. After 3 μs of axial acceleration, the current sheet moves occasionally to $z = 6$ cm at $t = 4.5$ μs.

Effects of p_0 can be derived by contrasting the result of case-1 versus 4, case-2 versus 5 or case-3 versus 6. It is straightforwardly to make the conclusion that higher p_0 can promote the formation a magnetic-impermeable current sheet faster and better.

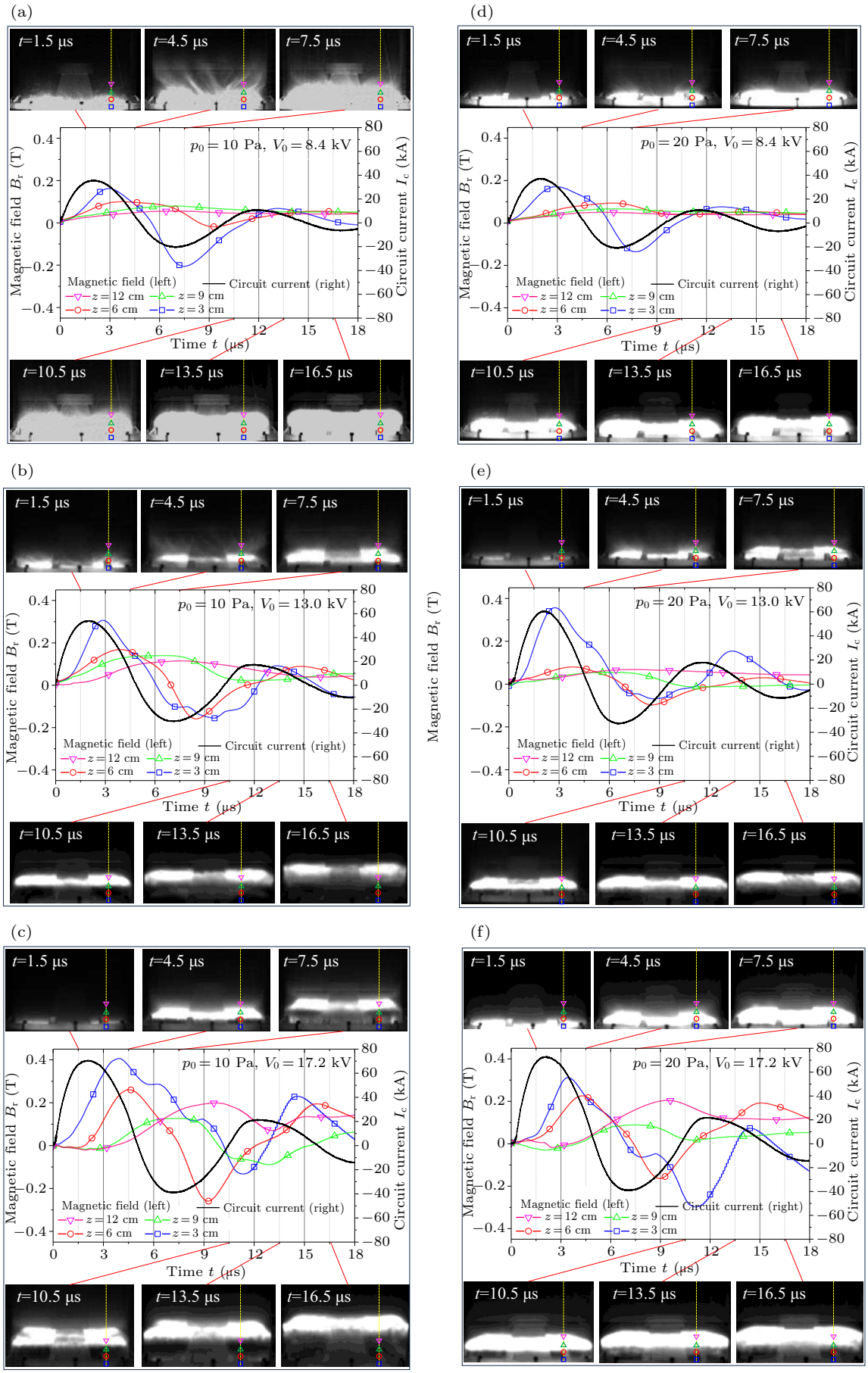


Fig. 13. Time-dependent B_r curves under varied discharge voltage V_0 and ambient fill pressure P_0: (a) case-1 ($p_0 = 10$ Pa, $V_0 = 8.4$ kV), (b) case-2 ($p_0 = 10$ Pa, $V_0 = 13.0$ kV), (c) case-3 ($p_0 = 10$ Pa, $V_0 = 17.2$ kV), (d) case-4 ($p_0 = 20$ Pa, $V_0 = 8.4$ kV), (e) case-5 ($p_0 = 20$ Pa, $V_0 = 13.0$ kV), (f) case-6 ($p_0 = 20$ Pa, $V_0 = 17.2$ kV).

4. Theoretical analysis

4.1. Gas ionization and plasma compression

The most apparent difference of case-1 from other five cases might be the crown-like ununiform branches shown in the high-speed photograph at $t = 4.5$ μs. Indeed, similar phenomenon can be found in case-2 at the same occasion where the ununiformity is much smaller. The branches are the results of ununiform gas breakdown far away from drive-coil, which is dominated by the angular electric field E_θ.

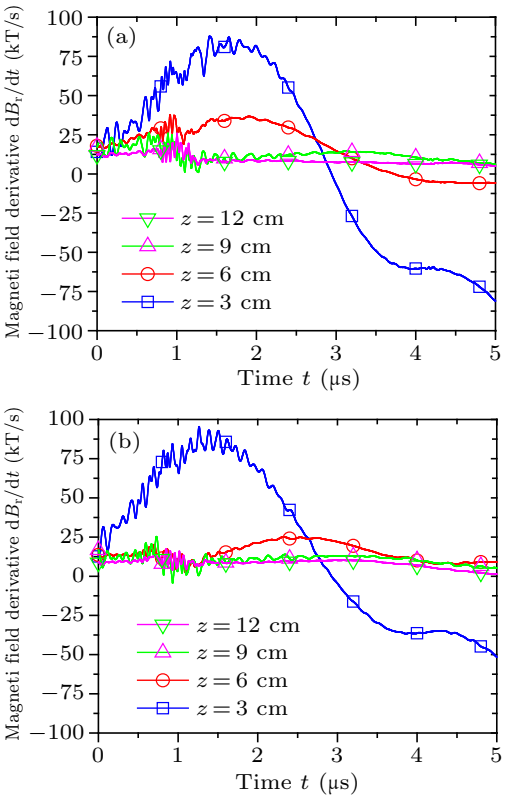


Fig. 14. Comparisons of the time rate of change of radial magnetic field dB_r/dt, which can be used as indicators to induced azimuthal electric field E_θ. (a) Case-1 ($p_0 = 10$ Pa, $V_0 = 8.4$ kV), (b) case-4 ($p_0 = 20$ Pa, $V_0 = 8.4$ kV).

According to Faraday's law, ignoring the effect of axial magnetic field, the magnitude of E_θ is proportional to the time rate of change of magnetic field intensity dB_r/dt. The curves of dB_r/dt at the early times of discharge for case-1 and case-4 are compared in Fig. 14. It can be concluded that, at both $t = 1.5$ μs and $t = 4.5$ μs, in case-2, the value of dB_r/dt at $z = 6$ cm remains over 1/5 of the value at $z = 3$ cm, while in case-4, the value of dB_r/dt at $z = 6$ cm is almost zero.

For those cases whose initial gas breakdown is insufficient (case-1, for instance), the magnetic field of drive-coil can diffusive far into the neutral gas across the relatively uncompact plasma current sheet. As a result, the induced angular electric field E_θ, which is generated by the time-varying magnetic field according to Faraday's law, remains sufficient to ionize the neutral gas far from drive-coil. However, owes to the partial screening effect of plasma current sheet, the intensity of E_θ is rather ununiform and the ionization is ununiform as well, exhibiting a crown-like branches of ionization region. For other cases whose initial gas breakdown is sufficient, the field is perfectly screened under plasma and the ionization region exhibits flat and compact appearance.

4.2. Energy deposition and conversation

The structure of the plasma current sheet evolves along with the discharge process. Its uniformity and compactness affect the magnetic field permeating into plasma and turns out to influence the deposition of pulse energy into plasma and the conversion into macroscopic kinetic energy.

In our previous research,[15] the coupling strength and energy deposition between circuit and plasma were quantified according to circuit parameters. The primary results are cited in Fig. 15, where the Lovberg ratio L^* evaluates the EM coupling strength between circuit and plasma, the energy deposition ratio ε represents the fraction of pulse energy deposited into plasma, and the exhaust velocity v_t shows the acceleration effects of propellant.

Combining the trend in Fig. 15 with the magnetic field characteristics obtained in this study, further insight into the physical mechanism of IPPTs can be derived:

The annular plasma current sheet induced by drive-coil weakens the magnetic field downstream and meanwhile, compress and strengthen the field between current sheet and drive-coil. The higher ionization degree of plasma, the larger conductivity and the more obvious shielding effect.

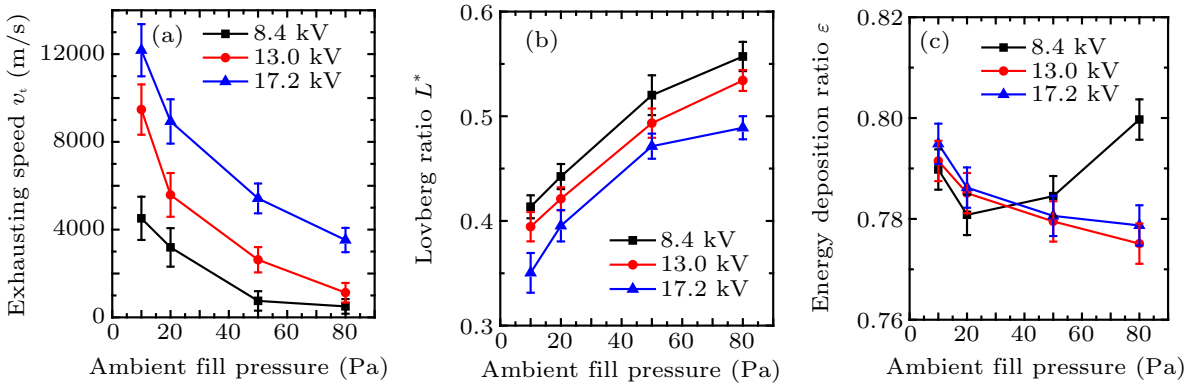


Fig. 15. Comparisons of derived parameters: (a) exhausting speed v_t, (b) Lovberg ratio L^*, (c) energy deposition ratio ε.

Under higher V_0, not only the initial induced electric field intensity is higher, but also the magnetic field intensity is higher. The former causes the propellant to be rapidly and efficiently ionized in the early stage of discharge, while the latter causes the plasma to be compressed into a flatter and compactor sheet form. Due to the extremely low EM field intensity above current sheet, the ionization region is restricted to a thin layer almost overlaps the current sheet. The current sheet then sweeps away the neutral gas it encountered just like a "snowplow".

A schematic of this snowplow deposition mode is illustrated in Fig. 16(a). In this mode, the mutual inductance between drive-coil and plasma is stronger, the proportion of energy used to ionize the gas is smaller. The Lorentz force is more concentrate and the utilization of the propellant is more sufficient. All of these effects make us believed that, a high performance IPPT device, like PIT Mark-Va, should operate in a snowplow mode.

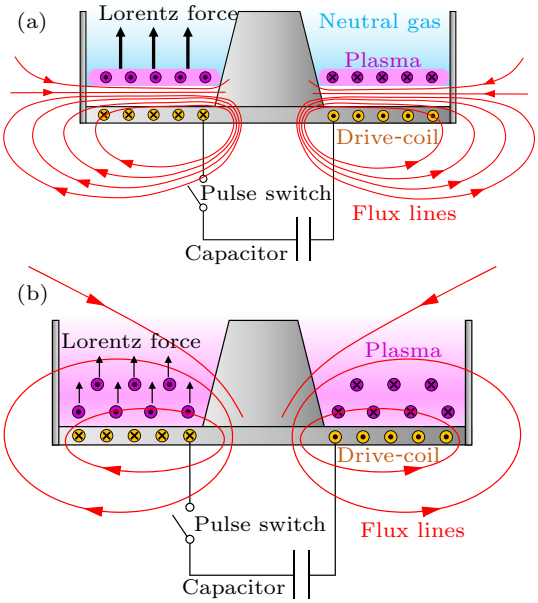


Fig. 16. Schematics of different energy deposition modes: (a) snowplow deposition mode, (b) diffusive deposition mode.

As is shown in Fig. 16(b), under lower V_0, it is difficult to achieve sufficient ionization at the early stage, and it is also more difficult to achieve effective compression of plasma during the successive stages of discharge. Most of the time, the EM field can penetrate deep into the propellant and as a result, a diffusive region of ununiform ionization emerges, for instance, the forementioned crown-like plasma branches. In this diffusive deposition mode, the mutual inductance between drive-coil and plasma is relatively small, the distribution of Lorentz force is more dispersed, and a large amount of energy is costed for propellant ionization. As a result, only small amount of energy is conversed into macroscopic kinetic energy which can produce actual thrust effect. This diffusive deposition mode can be found in most of the recent low-energy and low-performance variants of IPPT.[11,15–17]

Larger p_0 can provide more atoms to be ionized, which turns out to enhance the conductivity of plasma and promotes the establishment of a magnetic-impermeable current sheet. However, under ambient fill condition in this study, larger p_0 generally refers to bigger mass of bit been accelerated, which may cause slower acceleration of the plasma and consequently leads to abundant energy been dissipated through plasma resistance. This phenomenon has been discussed employing the dynamic matching theory in earlier researches, for more details one may refers to Refs. [18,19].

5. Conclusions

In this paper, a magnetic field diagnostic system for IPPT is constructed and calibrated. Combining magnetic diagnosis, high-speed photographing and electrical parameter measurement, a study about the correlation between plasma structure evolution and magnetic field permeability is conducted.

The results indicate that the formation of a flat and compact plasma current sheet at the early stage of discharge can effectively inhibit the magnetic field penetration into plasma. However, establishing such a magnetic-impermeable current sheet is much more difficult than pure gas ionization, which requires higher neutral gas pressure and larger discharge voltage. The shielding effect of plasma current sheet on coil magnetic field is conducive to increasing the deposition of pulse energy to plasma, but the conversion of pulse energy to macroscopic directional kinetic energy is further constrained by the dynamic matching state of current discharge waveform and the acceleration process of current sheet.

This study deepened the understanding of the internal physical mechanism of IPPT. The conclusions and findings can be referred to guide the design and optimization of high performance IPPTs.

Acknowledgements

Project supported by the Science Fund for Creative Research Groups of the National Natural Science Foundation of China (Grant No. T2221002) and the Young Scientists Fund of the National Natural Science Foundation of China (Grant No. 12305286).

References

[1] Polzin K A, Martin A, Little J, *et al.* 2020 *Aerospace* **7** 105
[2] Meyer M, Johnson L, Palaszewski, *et al.* 2012 *NASA Technique Report* **2021** 217641
[3] Robert H F and Mikellides P G 2005 41*st AIAA/ASME/SAE/ASEE Joint Propulsion Conference and Exhibit*, July 10–13, 2005, Tucson, Arizona

[4] Zheng P, Wu J J, Zhang Y, *et al.* 2020 *Int. J. Aerosp. Eng.* **1** 21
[5] Polzin K A 2011 *J. Propuls. Power* **27** 513
[6] Lovberg R H and Dailey C L 1982 *AIAA Journal* **20** 971
[7] Dailey C L and Lovberg R H 1993 *NASA Contractor Report* **1** 9291
[8] Dailey C L and Lovberg R H 1988 AFOSR *Technique Report* **89** 0130
[9] Russell D, Poylio J, *et al.* 2004 *Space Conference & Exhibit*, September 28–30, 2013, San Diego, California
[10] Lovberg R H and Dailey C L 1989 *AIAA/ASME/SAE/ASEE 25th Joint Propulsion Conference*, July 10–12, 1989, Monterey, CA, USA
[11] Polzin K A and Choueiri E Y 2015 *J. Propuls. Power* **22** 611
[12] Little J M, Mcculloh G I and Cameron M 2022 *J. Appl. Phys.* **9** 132
[13] Polzin K A, Hill C S, Turchi P J, *et al.* 2017 *J. Propuls. Power* **33** 659
[14] Li X K, Che B X, *et al.* 2020 *Chin. Phys. B* **29** 115201
[15] Bathgate N 2017 *Plasma Sci. Technol.* **19** 083001
[16] Sekine H, Koizumi H, *et al.* 2019 36th *International Electric Propulsion Conference*, September 15–20, 2019, Vienna, Austria
[17] Hallock A K, Martin A K, Polzin K A, *et al.* 2015 *IEEE Trans. Plas. Sci.* **43** 433
[18] Polzin K A 2008 *IEEE Trans. Plas. Sci.* **36** 2189
[19] Polzin K A and Choueiri E Y 2006 *IEEE Trans. Plas. Sci.* **34** 945